

pubs.acs.org/NanoLett Letter

# Signature of Correlated Insulator in Electric Field Controlled Superlattice

Jiacheng Sun, Sayed Ali Akbar Ghorashi, Kenji Watanabe, Takashi Taniguchi, Fernando Camino, Jennifer Cano, and Xu Du\*



Cite This: https://doi.org/10.1021/acs.nanolett.4c03238



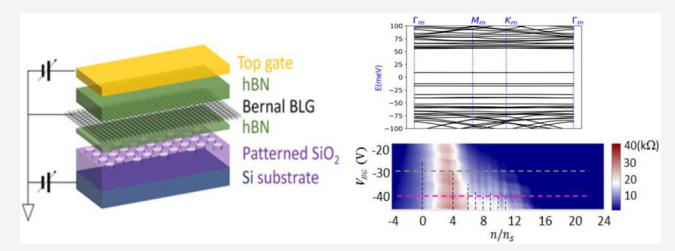
**ACCESS** 

III Metrics & More

Article Recommendations

s Supporting Information

ABSTRACT: On a two-dimensional crystal, a "superlattice" with nanometer-scale periodicity can be imposed to tune the Bloch electron spectrum, enabling novel physical properties inaccessible in the original crystal. While creating 2D superlattices by means of nanopatterned electric gates has been studied for band structure engineering in recent years, evidence of electron correlations—which drive many problems at the forefront of physics research—remains to be uncovered. In this work, we demonstrate signatures of a correlated insulator phase in Bernal-stacked bilayer graphene



modulated by a gate-defined superlattice potential, manifested as resistance peaks centered at integer multiples of single electron per superlattice unit cell carrier densities. The observation is consistent with the formation of a stack of flat low-energy bands due to the superlattice potential combined with inversion symmetry breaking. Our work paves the way to custom-designed superlattices for studying band structure engineering and strongly correlated electrons in 2D materials.

KEYWORDS: bilayer graphene, correlated electrons, superlattice, quantum transport

he electronic properties of crystals originate from the Bloch states, which can be modified by the presence of an external periodic potential superimposed on top of the underlying crystal lattice. A highly celebrated example is the moiré heterostructure, formed by stacking two 2D crystals with a slight mismatch in lattice constants or with a slight rotation. The resulting superlattice (moiré pattern) induces a wide variety of charge transport phenomena, from single-particlenatured satellite resistance peaks and Hofstadter butterfly physics to the formation of flat energy bands and the associated phases driven by electron correlations, including superconductivity, 1-3 Chern insulators, 3-7 Mott insulators, 8-10 Wigner crystals, 11 and orbital ferromagnets. 3 Followed by the experimental discovery of correlated insulators and superconductivity in magic-angle twisted bilayer graphene (TBLG), a wide variety of twisted heterostructures have been identified to share similar or partially similar properties, including twisted trilayer graphene, 12-14 twisted double bilayer graphene (BLG), 15-18 twisted transition metal dichalcogenides, 11,19,20 etc. The commonality of these different moiré systems suggests the importance of the superlattice potential in the formation of flat bands and the electron correlations.

Beyond moiré superlattices, a different approach for creating a superlattice potential, which allows much higher flexibility in its geometry and symmetry, is by means of the electric field effect using a patterned gate. Realized through nanopatterning, it also bypasses the long-range strain-induced inhomogeneity problem common in the moiré heterostruc-

tures.26 Understanding the impact of such superlattice potential in the absence of a moiré pattern provides valuable insight into the origin of some of the exotic behaviors observed in the twisted bilayer systems. Experimentally, effective realization of a gate-induced superlattice potential has been challenging due to the small pitch size required for the superlattice. To effectively modify the Bloch states, the pitch size must be much smaller than the phase coherence length. And for the estimated superlattice energy scale of  $\sim hv_F/a$  (h is Planck's constant,  $v_F$  is the Fermi velocity, and a is the lattice constant of the superlattice potential) to be sufficiently larger than the potential fluctuations, a pitch size of no more than a few tens of nanometers is required. With the developments of nanolithography, high 2D material device quality, and ultrathin 2D insulators such as hexagonal boron nitride (hBN), recent experimental works have demonstrated  $2D^{21,25}$  and one-dimensional  $(1D)^{22}$  superlattice potentials through gate dielectric patterning in monolayer graphene samples, with a superlattice periodicity as small as 16 nm.<sup>23</sup> In these devices, the superlattice potential has been shown to induce satellite Dirac points. However, since a Bravais superlattice always

Received: July 8, 2024
Revised: October 11, 2024
Accepted: October 16, 2024



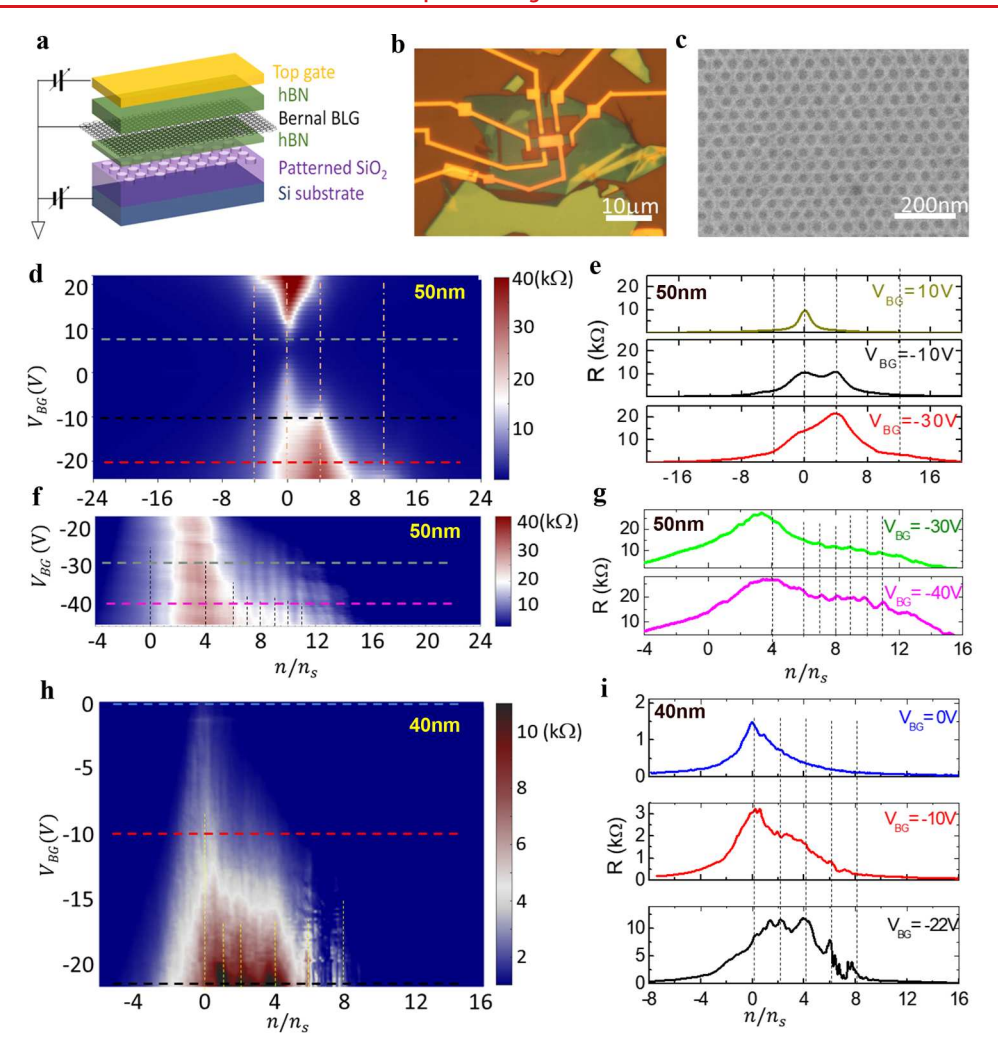


Figure 1. Dual-gated Bernal-stacked BLG samples and basic characteristics. a. Schematic of the sample structure. b. Optical micrograph of the sample with a 50 nm-pitch superlattice. c. Scanning electron microscope image of the patterned SiO<sub>2</sub> surface, showing a triangular lattice with a 50 nm pitch. d. Color-coded zero-magnetic field resistance as a function of mean carrier density and back gate voltage, measured with an excitation current of 100 nA. Here the averaged carrier density is normalized to the number of electrons per superlattice unit cell. The vertical dotted lines indicate the mean carrier densities where resistance peaks are observed. The horizontal line-cuts of the plots labeled by the colored dotted lines are presented in plot e, following the same order and with the same colors. In plot f, the 50 nm pitch sample is remeasured at large negative back gate voltages and a small excitation current of 10 nA. Signatures of flat bands and the correlated insulator are evident from the comb-like stripes (highlighted by the dotted lines), which correspond to resistance peaks, situated at integer multiples of a single charge per superlattice unit cell. The line-cuts of the plot with colored dashed lines are shown in plot g. In plot h, similar signatures of superlattice bands and correlated insulator phase are also observed in the 40 nm-pitch sample, where resistance peaks at multiples of two charges per superlattice unit cell (full- and half-fillings) are observed. The line-cuts of the plot at colored-dashed lines are shown in plot i. Similar to the 50 nm pitch sample, the most prominent superlattice-associated features are observed under negative back gate voltages. A full resistance map covering positive back gate voltages can be found in the Supporting Information. All measurements were taken at a temperature of 300 mK.

preserves 2-fold rotational symmetry, such a potential applied to monolayer graphene cannot gap the Dirac cone, which limits its ability to create flat energy bands and achieve correlated electron phases. This is not the case for Bernalstacked BLG in the presence of a superlattice potential, which has been recently proposed as a realistic platform to realize tunable flat energy bands<sup>27</sup> and host correlated phases.<sup>28</sup> In this work, we demonstrate the tuning of the electronic properties of BLG by a superlattice potential by using the dielectric patterning approach. In particular, we observe the evidence of a strongly correlated insulator phase purely from the applied superlattice potential (without a twist between the two layers as in the moiré bilayer systems), which is a major advancement from the previous studies of the noninteracting physics in a gate-defined superlattice.

The samples studied in this work are Bernal-stacked BLG encapsulated in hBN layers placed on  $SiO_2$  (285 nm)/Si substrates, with a triangular lattice of antidots  $\sim$ 50 nm deep patterned onto the surface of  $SiO_2^{21}$  (Figure 1a, b, c). Samples with two different superlattice pitch sizes, 40 and 50 nm, are fabricated and characterized. In the presence of a back gate voltage between the BLG and the conducting Si substrate, a periodic electric field contrast is formed as a result of the difference in dielectric constants where the encapsulated BLG sits on  $SiO_2$  ( $\epsilon_{SiO_2} \approx 4$ ) versus where it sits over an antidot ( $\epsilon_{vacuum} = 1$ ). Significant superlattice potential strength can be achieved when the bottom hBN thickness is much smaller than the diameter of the antidot (Supporting Information). A metal film top gate on the top hBN allows uniform tuning of the carrier density and Fermi energy throughout the BLG channel.

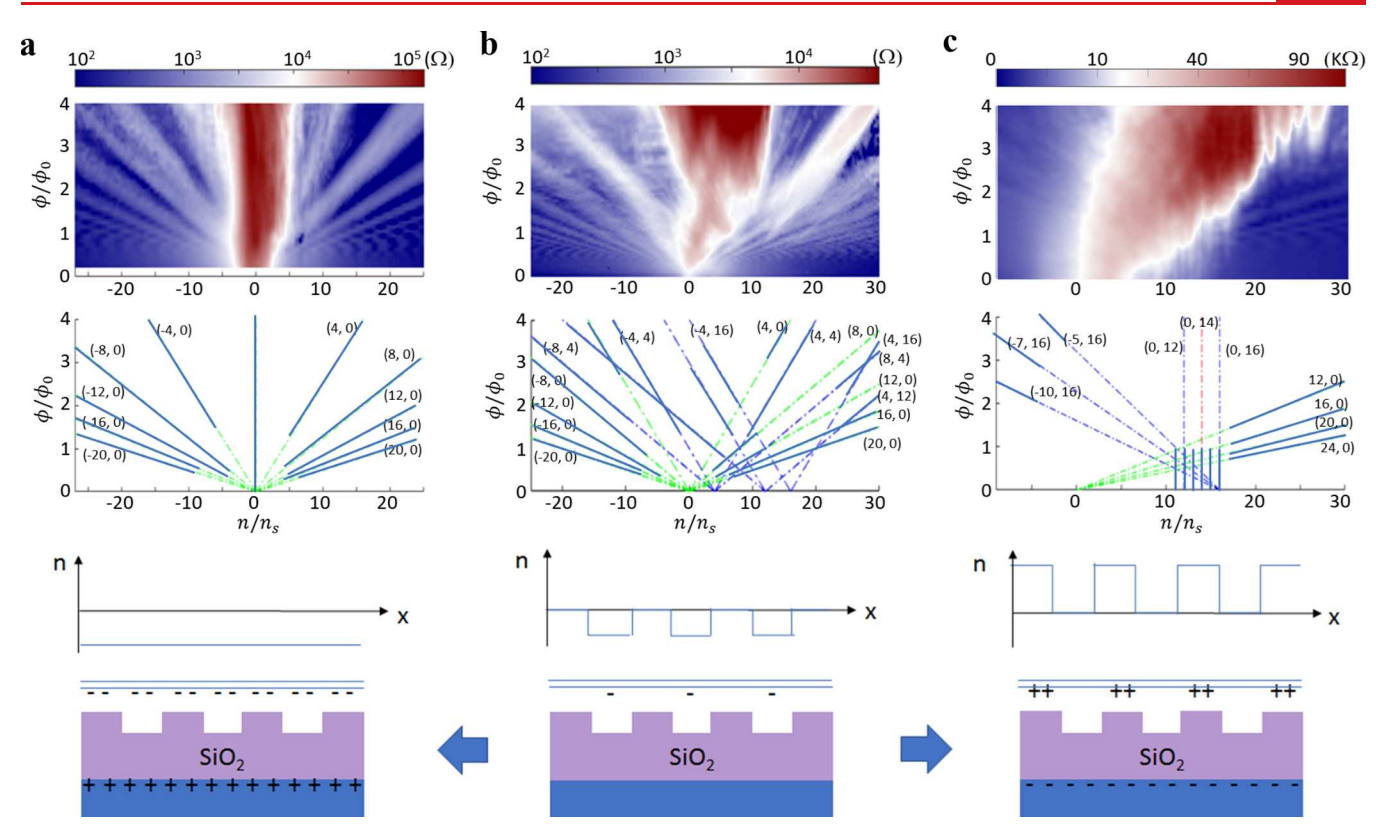


Figure 2. Landau fan diagrams under different superlattice potential profiles for the 50 nm-pitch sample, at back gate voltages of  $V_{BG}=15$  V (a), 0 V (b), and -30 V (c). At zero back gate, Landau fans from Bernal-stacked BLG (s=0) as well as a few side bands (s=4, 12, 16) can be identified. The superlattice-associated features may be attributed to unintentional doping, which is effectively patterned by the superlattice structure, with BLG locally electron-doped at the locations of the antidots. The unintentional doping profile is flattened under a mild positive back gate voltage, when higher electron density is gate-induced between the antidots, compensating the unintentional electron doping at the antidots. This results in conventional Landau fans for the Bernal-stacked BLG. Under a negative back gate voltage, the superlattice potential is enhanced, giving rise to different Landau fan patterns. For all back gate voltages, the Landau fan lines are calculated from the Diophantine equation and labeled by (t,s). The solid blue lines label the resistance valleys in the color-coded resistance plots, and the green dotted lines are their extrapolations. All the measurements were taken at a temperature of 300 mK.  $\phi_0$  corresponds to B=1.905 T for the 50 nm superlattice.

The difference between the top and the bottom gates also induces a displacement field, which manifests the differential doping on the two graphene layers. In BLG, the band structure is tuned by both the superlattice potential and the displacement field, while the Fermi energy is controlled by the overall doping. The two gate electrodes allow access to part of the parameter space with the superlattice potential and displacement field coadjusted by the back gate. The top gate tunes the overall Fermi energy as well as the displacement field. To find out the gate dependences of all the potential parameters, we combine the contribution of each gate to each graphene layer, considering an approximate screening efficiency of  $\alpha \sim 0.7$ : ~70% of the gate induced charge is on the adjacent graphene layer, and ~30% of the charge is on the remote graphene layer.<sup>29</sup> The gate dependence of the superlattice potential and displacement field is discussed in detail in the Supporting Information.

Figure 1d plots the dependence of electrical resistance on the mean carrier density and the back gate voltage for the 50 nm-pitch sample. Here the mean carrier density is normalized to the number of electrons per superlattice unit cell  $n/n_s$ , where  $n_s = \frac{2}{\sqrt{3} a^2} = 4.6 \times 10^{10} \text{ cm}^{-2}$  (a = 50 nm) corresponds to one electron per superlattice unit cell. Under minimum back gate voltages, a single resistance peak appears at the primary chargeneutral point, as expected for intrinsic Bernal-stacked BLG.

High carrier mobility and long coherence length can be inferred from the gate dependence of resistivity (Supporting Information). Increasing the back gate voltage amplitude, the charge-neutral resistance maximum increases as a result of inversion symmetry breaking from the displacement field, which opens up a band gap. <sup>30–32</sup> At the same time, additional resistance peaks emerge at mean carrier densities equal to integer multiples of  $4n_s$ , most noticeable at  $4n_s$  and  $12n_s$ . This is consistent with the formation of energetically isolated superlattice bands with 4-fold (spin and valley) degeneracy. We note the absence of a resistance peak at  $8n_s$ , which suggests that the second and third superlattice bands from the original charge neutrality are not effectively energetically isolated. The superlattice-induced features are significantly more pronounced on the electron side. Similar particle-hole asymmetry has been observed in monolayer graphene under superlattice potential,<sup>21</sup> which can be attributed to the asymmetry in the minima/maxima of the triangular superlattice potential; that is, the electrons in the conduction band localize in the potential minima, which form a honeycomb lattice, while the holes in the valence band localize in the potential maxima, which form a triangular lattice. In the case of BLG, additional asymmetry may also come from the gate dependence of the displacement field. We also observed that the primary resistance peak (n =0) becomes overwhelmed by that from the superlatticeinduced band gap at  $\frac{n}{n} = 4$  under moderate negative back gate

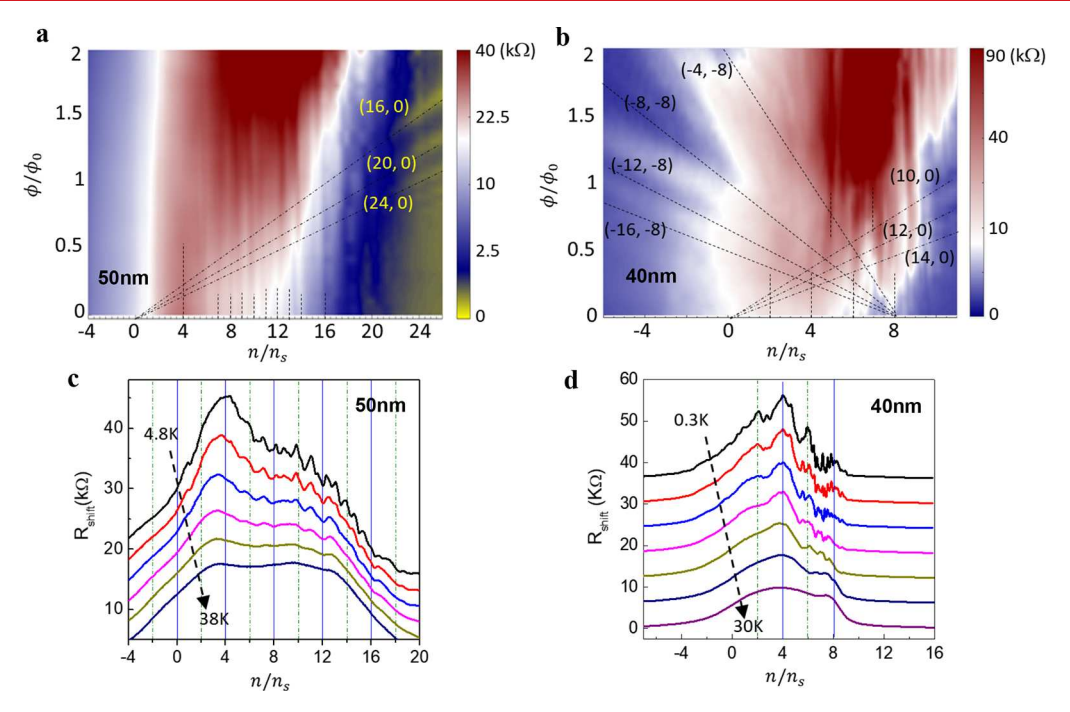


Figure 3. Magnetic field and temperature dependences of the signatures of the correlated insulator phase. **a** and **b** plot the Landau fan diagrams of the 50 nm-pitch sample (at a back gate voltage of -42 V) and the 40 nm-pitch sample (at a back gate voltage of -20 V), respectively. The fan lines associated with Bernal-stacked BLG can be identified, which extrapolate to the origin. At lower densities, resistance peaks corresponding to the integer and fractional filling of the superlattice bands are observed and are highlighted by dotted lines.  $\phi_0$  corresponds to B = 1.905 T for the 50 nm superlattice and B = 2.976 T for the 40 nm superlattice. **c** and **d**. Temperature dependence of the resistance peaks for the 50 nm- and 40 nm-pitch samples, respectively. In **c**, the curves from top to bottom correspond to temperatures of 4.8, 8, 12, 19, 28, and 38 K. In **d**, the curves from top to bottom correspond to temperatures of 0.3, 1, 2, 4, 8.5, 15, and 30 K.

voltage (Figure 1d, e). This is very different from what was observed in superlattice-modulated monolayer graphene<sup>21</sup> and is explained later in the discussion of band structure modeling. The superlattice-induced resistance peaks are significantly more pronounced under negative back gate voltages. As discussed below, this can be explained by the unintentional charge doping which is modulated by the patterned  $SiO_2$  surface, enhancing the potential strength for  $V_{BG} < 0$ . In the discussions below, we focus on the data taken under negative  $V_{BG}$ .

With the negative back gate voltage further pushed to larger values, we explore the strong superlattice potential regime, where a striking feature becomes evident in the gate dependence of resistance, shown in Figure 1f, g (taken at a slower top gating ramping speed and smaller excitation current compared to those in Figure 1d). A comb-like set of resistance peaks emerges at integer multiples of a single electron per superlattice unit cell, most evidently at  $\frac{n}{n}$  = 6, 7, 8, 9, ..., 12 at a back gate voltage between -30 V and a maximum applied value of -42 V. These resistance peaks correspond to not only full- but also half- and quarter-fillings of the superlattice energy bands, signifying an interaction effect that breaks the 4-fold degeneracy of each superlattice band, resulting in correlated insulating behavior at the Coulomb gaps, similar to what observed in magic angle TBLG. Unlike in magic angle TBLG, the filling factors here show a wide range of values which would correspond to a stack of flat energy bands.

The superlattice bands and correlated insulator phase are further confirmed in a 40 nm-pitch sample, which displays qualitatively similar behaviors to those in the 50 nm-pitch sample (Figure 1h, i), with  $n_s = \frac{2}{\sqrt{3} a^2} = 7.2 \times 10^{10} \text{ cm}^{-2}$  ( $a = \frac{2}{\sqrt{3} a^2} = 7.2 \times 10^{10} \text{ cm}^{-2}$ 

40 nm). Here again, under moderate negative back gate voltage the primary n = 0 resistance peak becomes overwhelmed by the nearest superlattice band gap at  $\frac{n}{n_s} = 4$ . Under relatively

large negative back gate voltages, we also observed resistance peaks at half-filled superlattice bands, similar to the correlated insulating behavior at the Coulomb gaps observed in magic angle TBLG. The slight misalignment of some of the resistance peaks with their corresponding nominal filling factors, in both samples, may be attributed to the uncertainty in the gate capacitance. The small quantum capacitance due to the low density of states, for example, may lead to a slight gate dependence of the gate capacitance.

Compared to the prior reports on moiré superlattices, the gate-defined superlattice charge transport features observed here are significantly less pronounced. A main reason for the "smearing" of the superlattice features is the large superlattice unit cell size (~10 times larger area than that of a typical moiré superlattice), which results in the density associated with the filling of a superlattice band being small (~10 times smaller than that of a typical moiré superlattice) and even becomes comparable to the random carrier density fluctuations (see Supporting Information). On the other hand, the fact that mean carrier densities at which the resistance peaks scale with the superlattice unit cell area is strongly indicative of their origin being associated with the superlattice-induced flat energy bands.

To further study the superlattice-induced energy bands, we next turned to quantizing magnetic fields. In the absence of a superlattice potential, we expect the conventional Landau level sequence associated with the Bernal-stacked BLG. This is observed under moderate positive back gate voltages, where

 $R_{xx}$  shows resistance valleys in the Landau fan diagram displaying a filling factor sequence of v=4N (N is an integer), as shown in Figure 2a for the 50 nm-pitch sample. Under zero back gate voltage, however, we observed additional Landau fan features that originate from the superlattice bands. In Figure 2b, the carrier density and magnetic flux dependence of the  $R_{xx}$  valleys are compared to calculations from the Diophantine equation:  $\frac{n}{n_s} = t \frac{\phi}{\phi_0} + s$ . Here  $\phi = B/n_s$  is the magnetic flux quantum; and t and s are integers that correspond to the number of electrons per magnetic flux quantum and per superlattice unit cell, respectively. The Landau fan lines, labeled as (t, s), originate from s = 4N, indicating the noninteracting nature of the superlattice bands under weak periodic potential.

The presence of superlattice bands at zero back gate voltage suggests a "residual" superlattice potential. One possible scenario is that the BLG is locally electron-doped at locations of the SiO<sub>2</sub> antidots. In the presence of a mild positive back gate voltage, the superlattice induced by the back gate (which induces lower electron density at the locations of the antidots than in between the antidots, due to the dielectric constant contrast) would compensate and smooth out the superlattice potential. This explains why the superlattice potential associated features in the Landau fan diagram disappear under a moderate positive back gate voltage, but appear under zero back gate voltage, as shown in Figure 2. A detailed discussion on the charge distribution in the BLG and estimation on the gate voltage for smoothening of the residue superlattice potential can be found in the Supporting Information.

Under large negative back gate voltages, we expect a strong superlattice potential and displacement field. There, the Landau fan diagram shows a pattern drastically different from that in the weak superlattice potential. The Landau fans with the conventional BLG sequence (s=0) do not extrapolate to a pronounced resistance at n, B=0. Besides these original Landau fans, vertical stripes corresponding to resistance peaks with t=0 are observed on the electron side of the resistance peak, as shown by the vertical lines in Figure 2c.

In Figure 3a and b, we focus on the Landau fan diagrams in the fractionally filled superlattice band regime for the 50 nmand 40 nm-pitch samples, respectively. In both diagrams, the zero magnetic field resistance peaks develop into vertical stripes nondispersive in the magnetic field. In the 50 nm-pitch sample, such features dominate over the fillings up to  $s \sim 15$ 20 (i.e., up to 5 superlattice bands) at a back gate voltage of -42 V. In the 40 nm-pitch sample at a back gate voltage of -25 V, the vertical stripes of resistance peaks correspond to fillings of s = 2, 4, 6, 8 in a low magnetic field. In a larger magnetic field, further symmetry breaking happens, which leads to the emergence of resistance peaks at fillings of s = 5, 7. At larger densities beyond the regime of the comb-like features, we observe Landau fans with s = 0, which trace to n = 0. On the hole side, we also observed Landau fans with 4-fold degeneracy, which extrapolate to s = 8.

In twisted bilayer systems, correlated behavior is commonly associated with the formation of flat energy bands, with diminishing kinetic energy and diverging density of states. With the gate-defined superlattice potential on BLG, it has been theoretically proposed that a stack of flat bands can form under large superlattice potential and displacement field.<sup>27</sup> Our

observation of resistance peaks at integer multiples of single and double electrons per superlattice unit cell over a wide range of carrier densities is consistent with the formation of such a stack of flat bands, with the signature of correlated insulator behavior they are associated with.

Figure 3c, d plot the temperature dependence of the resistance peaks at all the fillings for the 50 nm- and 40 nm-pitch samples, respectively. The resistance peaks associated with the Coulomb gaps in the half- or quarter-filled superlattice bands become thermally smeared at ~20 K, while the resistance peaks associated with the noninteracting band gaps persist up to much higher temperatures. At the lowest temperatures, weaker universal conductance fluctuations (UCFs) are also observed. UCFs can be distinguished from the superlattice-associated peaks by their different back gate dependence and thermal cycling response (Supporting Information).

To understand our experimental observations, we study Bernal-stacked BLG in the presence of a superlattice potential and a displacement field using a four-band continuum model (consisting of two layers and two spins) with an applied 2D cosine potential. Specifically, the Hamiltonian takes the form

$$H = H_{BLG} + H_{SL} + H_{V}$$

The intrinsic Bernal-stacked BLG term is represented as

$$H_{BLG} = \hbar v_F (\chi k_x \sigma_x + k_y \sigma_y) + \frac{t}{2} (\tau^1 \sigma_x - \tau^2 \sigma_x)$$

where  $\chi=\pm$  is the valley index,  $\nu_{\rm F}$  is the Fermi velocity of graphene, k is the electron crystal momentum, and t is the interlayer coupling; Pauli matrices  $\tau$  and  $\sigma$  correspond to the layer and sublattice spaces. The spatially modulated superlattice potential is described by

$$H_{SL} = \frac{1}{2} \begin{bmatrix} V_{SL}^{(1)} \sigma_0 & 0_2 \\ 0_2 & V_{SL}^{(2)} \sigma_0 \end{bmatrix} \sum_{n=1}^{6} \cos(Q_n \cdot r)$$

where  $V_{SL}^{(1),(2)}$  are the effective strength of the superlattice potential on each layer and  $Q_n$  are its wavevectors. For a triangular superlattice potential the mini-Brillouin zone is defined by  $Q_n = Q\left(\cos\left(\frac{2n\pi}{6}\right), \sin\left(\frac{2n\pi}{6}\right)\right)$ , which define the high-symmetry points  $\Gamma_m = (0,0), M_m = \frac{1}{2}Q_0$ , and  $K_m = \frac{1}{3}(Q_0 + Q_1)$ .

Finally, the mean potential can be captured by

$$H_{V} = \begin{bmatrix} V_{0}^{(1)} \sigma_{0} & 0_{2} \\ 0_{2} & V_{0}^{(2)} \sigma_{0} \end{bmatrix}$$

where mean potentials on the two graphene layers  $V_0^{(1),(2)}$  are contributed from the gates and the unintentional doping.

Our numerical calculations case-study the superlattice bands for the 50 nm-pitch sample. All the gate-induced potential parameters on each graphene layer are estimated based on the electrostatic simulations of the actual device structure (see Supporting Information). The superlattice potential is also contributed by an unintentional doping from the back gate side, which can be represented as an effective back gate voltage  $V_D \sim 15~\rm V$ . The resulting potentials follow the empirical relations  $V_{SL}^{(1)} = 0.498(V_{BG} - V_D)$  [meV];  $V_{SL}^{(2)} = 0.213(V_{BG} - V_D)$  [meV];  $V_0^{(1)} = 1.17V_T + 2.73V_{BG} + 1.12V_D$  [meV]; and

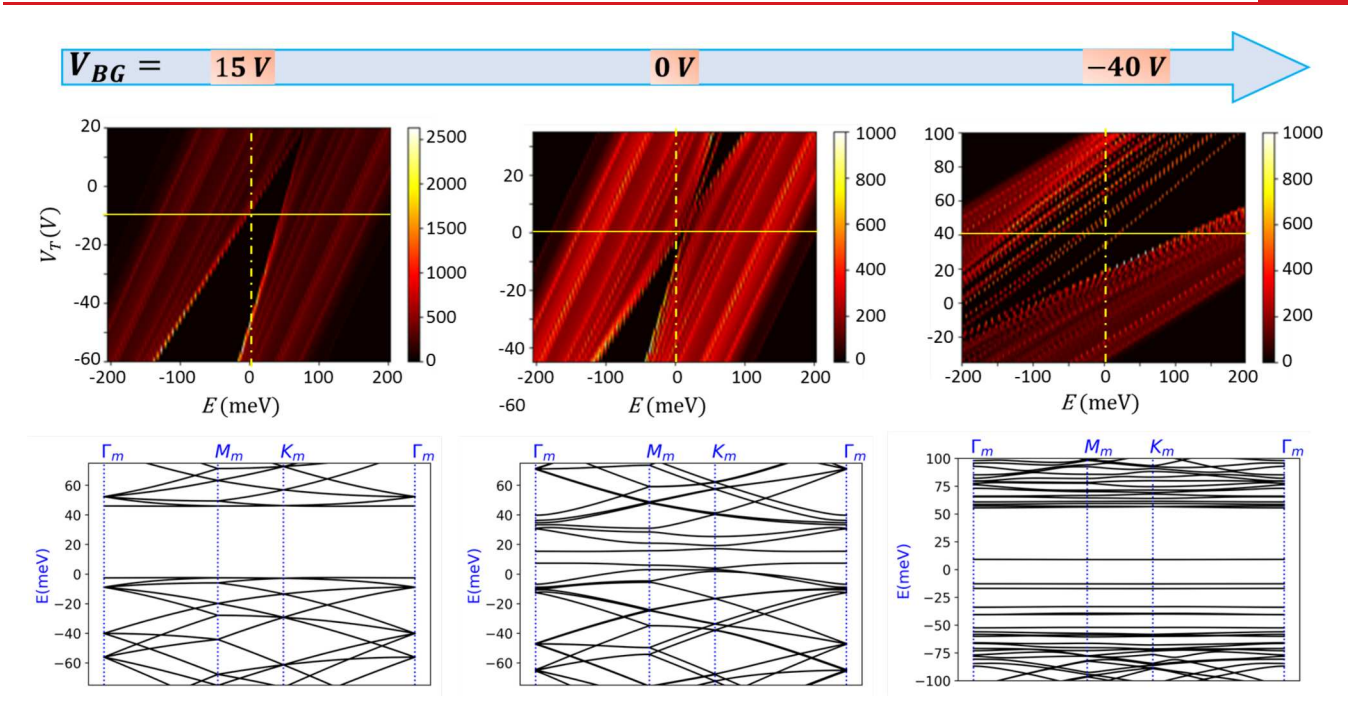


**Figure 4.** Calculated band structures and DOS at various back gate voltages for the 50 nm-pitch sample. The top row shows the color-coded DOS versus energy and  $V_T$ . The charge transport measurements are related to the DOS at the Fermi level indicated by the vertical dotted yellow lines at E = 0. The bottom row shows the band structures at  $V_T$  indicated by the solid yellow lines in the top row.

 $V_0^{(2)} = 2.73V_T + 1.17V_{BG} + 0.48V_D$  [meV]. Here  $V_T$  is the equivalent top gate voltage normalized by the back gate capacitance (over 285 nm-thick SiO<sub>2</sub>).

Based on the above model and parameters, we calculate the band structure and its evolution in  $V_{BG}$  (Figure 4). In the absence of a superlattice potential, the DOS plot at  $V_{BG}$  = 15 V shows an energy gap separating the energy continuums of conduction and valence bands, as expected for a Bernal-stacked BLG. On changing the back gate voltage toward negative values and hence increasing the superlattice potential strength, multiple flat energy bands emerge at low energies, showing up in the DOS plots as sharp lines, which indicate a narrow bandwidth. Each flat band is 4-fold (spin-valley) degenerate. The transport measurement compares to the zero-energy linecuts in the DOS plots. Insulating behavior at a filling  $n/n_s$  that is not a multiple of 4 indicates a correlated insulator that spontaneously breaks spin-valley symmetry. (We note that correlation-driven spontaneous symmetry breaking is not included in our band structure calculation.)

To trace the evolution of the superlattice bands under  $V_T$ , one can zoom into the vicinity of the charge neutrality regime in the DOS plot (see Supporting Information). Increasing the magnitude of  $V_{BG}$  at low superlattice potential and displacement field, the band gap between the first and the second superlattice bands increases faster than the band gap associated with the primary neutrality point, resulting in the resistance peak at  $\frac{n}{n_s} = 4$  to overwhelm the primary charge neutrality resistance peak. Also consistent with the experimental observation, the second and the third superlattice bands are nearly degenerate, resulting in the absence of a measurable resistance peak at  $\frac{n}{n} = 8$  in the 50 nm-pitch sample.

In summary, we have studied Bernal-stacked BLG under gate-defined tunable superlattice potential, which induces energetically isolated superlattice bands. Under strong super-

lattice potential, signatures of correlated insulator phases are observed, manifested as a set of resistance peaks centered at carrier densities of integer multiples of a single electron per unit cell of the superlattice potential. We attribute the correlated electrons to the formation of flat energy bands due to the superlattice potential combined with inversion symmetry breaking. Inducing correlated electron phases with nanopattern-defined electric gates paves the way to custom-designed superlattices with arbitrary geometries and symmetries for studying band structure engineering and strongly correlated electrons in 2D materials.

## ASSOCIATED CONTENT

# Supporting Information

The Supporting Information is available free of charge at https://pubs.acs.org/doi/10.1021/acs.nanolett.4c03238.

Sample fabrication, measurement setup and sample quality; charge distribution in bilayer graphene; electrostatic simulations; control measurement on bilayer graphene without superlattice potential; Hall effect; universal conductance fluctuations; superlattice band evolution; additional data: gate-dependent resistance under a 40 nm-pitch superlattice (PDF)

# AUTHOR INFORMATION

# **Corresponding Author**

Xu Du − Department of Physics and Astronomy, Stony Brook University, Stony Brook, New York 11794-3800, United States; orcid.org/0000-0001-5610-2338; Email: xu.du@ stonybrook.edu

#### Authors

Jiacheng Sun – Department of Physics and Astronomy, Stony Brook University, Stony Brook, New York 11794-3800, United States

- Sayed Ali Akbar Ghorashi Department of Physics and Astronomy, Stony Brook University, Stony Brook, New York 11794-3800, United States
- Kenji Watanabe Research Center for Electronic and Optical Materials, National Institute for Materials Science, Tsukuba 305-0044, Japan; orcid.org/0000-0003-3701-8119
- Takashi Taniguchi Research Center for Materials Nanoarchitectonics, National Institute for Materials Science, Tsukuba 305-0044, Japan; orcid.org/0000-0002-1467-3105
- Fernando Camino Center for Functional Nanomaterials, Brookhaven National Laboratory, Upton, New York 11973, United States
- Jennifer Cano Department of Physics and Astronomy, Stony Brook University, Stony Brook, New York 11794-3800, United States; Center for Computational Quantum Physics, Flatiron Institute, New York, New York 10010, United States

Complete contact information is available at: https://pubs.acs.org/10.1021/acs.nanolett.4c03238

#### Notes

The authors declare no competing financial interest.

### ACKNOWLEDGMENTS

X.D. acknowledges support from NSF awards under Grant Nos. DMR-1808491 and DMR-2104781. K.W. and T.T. acknowledge support from the JSPS KAKENHI (Grant Nos. 20H00354, 21H05233, and 23H02052) and World Premier International Research Center Initiative (WPI), MEXT, Japan. S.A.A.G. and J.C. acknowledge support from the Air Force Office of Scientific Research under Grant No. FA9550-20-1-0260 and acknowledge hospitality from the Kavli Institute for Theoretical Physics, where this research was supported in part by the National Science Foundation under Grant No. NSF PHY-1748958. J.C. also acknowledges support from the Flatiron Institute, a division of the Simons Foundation, and the Alfred P. Sloan Foundation through a Sloan Research Fellowship. This research used the Electron Microscopy facility of the Center for Functional Nanomaterials (CFN), which is a U.S. Department of Energy Office of Science User Facility, at Brookhaven National Laboratory, under Contract No. DE-SC0012704.

# REFERENCES

- (1) Cao, Y.; et al. Unconventional superconductivity in magic-angle graphene superlattices. *Nature* **2018**, *556*, 43.
- (2) Yankowitz, M.; et al. Tuning superconductivity in twisted bilayer graphene. *Science* **2019**, *363* (6431), 1059–1064.
- (3) Lu, X.; et al. Superconductors, orbital magnets and correlated states in magic-angle bilayer graphene. *Nature* **2019**, *574* (7780), 653–657.
- (4) Serlin, M.; et al. Intrinsic quantized anomalous Hall effect in a moiré heterostructure. *Science* **2020**, *367* (6480), 900–903.
- (5) Nuckolls, K. P.; et al. Strongly correlated Chern insulators in magic-angle twisted bilayer graphene. *Nature* **2020**, *588* (7839), *6*10–615.
- (6) Chen, G.; et al. Tunable correlated Chern insulator and ferromagnetism in a moiré superlattice. *Nature* **2020**, *579* (7797), 56–61.
- (7) Xie, Y.; et al. Fractional Chern insulators in magic-angle twisted bilayer graphene. *Nature* **2021**, *600* (7889), 439–443.
- (8) Cao, Y.; et al. Correlated insulator behaviour at half-filling in magic-angle graphene superlattices. *Nature* **2018**, *556* (7699), 80–84.

- (9) Xu, Y.; et al. Correlated insulating states at fractional fillings of moiré superlattices. *Nature* **2020**, *587* (7833), 214–218.
- (10) Tang, Y.; et al. Simulation of Hubbard model physics in WSe2/WS2 moiré superlattices. *Nature* **2020**, *579* (7799), 353–358.
- (11) Regan, E. C.; et al. Mott and generalized Wigner crystal states in WSe2/WS2 moiré superlattices. *Nature* **2020**, *579* (7799), 359–363
- (12) Hao, Z.; et al. Electric field-tunable superconductivity in alternating-twist magic-angle trilayer graphene. *Science* **2021**, *371* (6534), 1133–1138.
- (13) Kim, H.; et al. Evidence for unconventional superconductivity in twisted trilayer graphene. *Nature* **2022**, *606* (7914), 494–500.
- (14) Christos, M.; Sachdev, S.; Scheurer, M. S. Correlated Insulators, Semimetals, and Superconductivity in Twisted Trilayer Graphene. *Physical Review X* **2022**, *12* (2), 021018.
- (15) Shen, C.; et al. Correlated states in twisted double bilayer graphene. *Nat. Phys.* **2020**, *16* (5), 520–525.
- (16) Wang, Y.; et al. Bulk and edge properties of twisted double bilayer graphene. *Nat. Phys.* **2022**, *18* (1), 48–53.
- (17) Rickhaus, P.; et al. Correlated electron-hole state in twisted double-bilayer graphene. Science 2021, 373 (6560), 1257–1260.
- (18) Liu, L.; et al. Isospin competitions and valley polarized correlated insulators in twisted double bilayer graphene. *Nat. Commun.* **2022**, *13* (1), 3292.
- (19) Devakul, T.; Crépel, V.; Zhang, Y.; Fu, L. Magic in twisted transition metal dichalcogenide bilayers. *Nat. Commun.* **2021**, *12* (1), 6730
- (20) Zhang, Z.; et al. Flat bands in twisted bilayer transition metal dichalcogenides. *Nat. Phys.* **2020**, *16* (11), 1093–1096.
- (21) Forsythe, C.; et al. Band structure engineering of 2D materials using patterned dielectric superlattices. *Nat. Nanotechnol.* **2018**, *13* (7), 566–571.
- (22) Li, Y.; et al. Anisotropic band flattening in graphene with one-dimensional superlattices. *Nat. Nanotechnol.* **2021**, *16* (5), 525–530.
- (23) Barcons Ruiz, D.; et al. Engineering high quality graphene superlattices via ion milled ultra-thin etching masks. *Nat. Commun.* **2022**, *13* (1), 6926.
- (24) Drienovsky, M.; et al. Commensurability Oscillations in One-Dimensional Graphene Superlattices. *Phys. Rev. Lett.* **2018**, *121* (2), 026806.
- (25) Huber, R.; et al. Gate-Tunable Two-Dimensional Superlattices in Graphene. *Nano Lett.* **2020**, 20 (11), 8046–8052.
- (26) Lau, C. N.; Bockrath, M. W.; Mak, K. F.; Zhang, F. Reproducibility in the fabrication and physics of moiré materials. *Nature* **2022**, *602* (7895), 41–50.
- (27) Ghorashi, S. A. A.; et al. Topological and Stacked Flat Bands in Bilayer Graphene with a Superlattice Potential. *Phys. Rev. Lett.* **2023**, *130* (19), 196201.
- (28) Krix, Z. E.; Sushkov, O. P. Patterned bilayer graphene as a tunable strongly correlated system. *Phys. Rev. B* **2023**, *107* (16), 165158.
- (29) Rokni, H.; Lu, W. Layer-by-Layer Insight into Electrostatic Charge Distribution of Few-Layer Graphene. *Sci. Rep.* **2017**, 7 (1), 42821.
- (30) Ohta, T.; et al. Controlling the Electronic Structure of Bilayer Graphene. *Science* **2006**, *313* (5789), 951–954.
- (31) Zhou, S. Y.; et al. Substrate-induced bandgap opening in epitaxial graphene. *Nat. Mater.* **2007**, *6* (10), 770–775.
- (32) Oostinga, J. B.; et al. Gate-induced insulating state in bilayer graphene devices. *Nat. Mater.* **2008**, *7* (2), 151–157.